

**Chandra observation of Abell 1689: New determination of mass
distribution and comparison to lensing measurements**

Sui-Jian Xue and Xiang-Ping Wu

National Astronomical Observatories, Chinese Academy of Sciences, Beijing 100012, China

Received November 00 2001; accepted April 25 2002

arXiv:astro-ph/0204510v1 30 Apr 2002

ABSTRACT

We present a new estimate of the projected X-ray mass of Abell 1689 observed with Chandra, in an attempt to clarify the issue of whether or not there exists a discrepancy between X-ray and gravitational lensing mass estimates claimed in previous investigations based on *Einstein*, *ROSAT* and *ASCA* observations. A particular attention is paid to examining if there is an offset between X-ray centroid and central dominant cD galaxy, which may be an indicator of the presence of local dynamical activities of intracluster gas in the central core and therefore, explain the discrepancy between X-ray and lensing mass estimates, if any. The unprecedentedly high spatial resolution achieved by Chandra allows us to precisely localize the X-ray centroid of Abell 1689, which appears to coincide perfectly with the central cD galaxy. This fact, along with the symmetry and regularity of the X-ray surface brightness and temperature distributions, suggests that Abell 1689 is a fully-relaxed cluster. We thus employ hydrostatic equilibrium hypothesis to determine the projected mass profile of Abell 1689, and compare it with the results obtained by different lensing techniques available in the literature. Our analysis confirms the existence of the discrepancy of a factor of ~ 2 between X-ray and lensing mass estimates in the central region of $r \approx 0.2$ Mpc, although the two methods yield essentially consistent result on large radii. If the perfect coincidence between the X-ray center and the cD galaxy of Abell 1689 detected by Chandra observation is not a projection effect, the central mass discrepancy between X-ray and lensing measurements may pose a challenge to our conventional understanding of dynamical evolution of the intracluster gas in the central regions of clusters.

Subject headings: galaxies: clusters: individual (Abell 1689) — dark matter —

gravitational lensing — X-ray: galaxies: clusters — X-ray: individual (Abell
1689)

1. Introduction

Clusters of galaxies serve as an ideal cosmological laboratory for test of theories of formation and evolution of structures, and for determinations of fundamental cosmological parameters such as the matter density parameter Ω_M , the baryon fraction f_b , the normalization parameters σ_8 and the shape parameter Γ . All these cosmological applications depend critically on how accurately the mass distributions of clusters can be measured. Current techniques include the optical measurements of distribution and velocity dispersion of cluster galaxies combined with the Jeans equation, the X-ray observations of intracluster gas (density and temperature profiles) coupled with the hydrostatic equilibrium hypothesis, and the gravitational lensing effects of distant galaxies behind clusters. Other methods such as the measurements of hot intracluster gas through the Sunyaev-Zeldovich effect and the numerical simulations of formation and evolution of clusters also act as a complementary manner to the above direct approaches. A comparison of different mass estimates provides a simple way to examine the reliability and accuracy of different methods, which also allows one to diagnose dynamical evolution of different matter components (galaxies, gas and dark matter) of clusters. In such an exercise, the mass distribution revealed by gravitational lensing, which is independent of the matter content and dynamical state of clusters, may be used as a reference point for judging other approaches. Previous studies have essentially arrived at the following conclusions: There is good agreement between the weak gravitational lensing, X-ray and optical determined cluster masses on large scales characterized by X-ray core radii, while in the central regions of some lensing clusters the X-ray method is likely to systematically underestimate cluster masses by a factor of ~ 2 (Wu 1994; Miralda-Escudé & Babul 1995; Wu & Fang 1997; Allen 1998; Wu et al. 1998; Wu 2000 and references therein). Because this discrepancy occurs in the very central cores of clusters, it may arise from our oversimplification of dynamical properties of the intracluster gas on small scales. Indeed, the discrepancy becomes significant only

for non-cooling flow clusters (Allen 1998; Wu 2000), in which the apparent offsets between X-ray and lensing centers have been detected (Allen 1998; Katayama, Hayashida & Hashimoto 2002). Therefore, detailed knowledge of the gas distribution in the inner regions of clusters will be crucial for clarifying the issue.

The unprecedentedly high spatial resolution of the Chandra X-ray Observatory has permitted detailed studies of intracluster gas in the innermost regions of clusters. So far, central X-ray masses have been explicitly derived for several lensing clusters observed with Chandra. For at least three clusters (Abell 1835, MS 1358 and Abell 2390), the newly determined X-ray masses are found to be in good agreement with the gravitational lensing measurements (Allen, Ettori & Fabian 2001; Schmidt, Allen & Fabian 2001; Arabadjis, Bautz & Garmire 2001), while a significant discrepancy between the X-ray and strong lensing mass estimates is also detected in Abell 2218 (Machacek et al. 2001). For the latter, the X-ray centroid shows an offset of $\sim 22''$ from the dominant cD galaxy. This reinforces the argument that the mass discrepancy may be attributed to the inappropriate use of hydrostatic equilibrium to the intracluster gas in the central regions where substructures and their bulk motion may govern the dynamical process of intracluster gas even if clusters become fully relaxed. Indeed, the existence of subsonic motion of central gas has been conformed recently by Chandra observation in cluster RXJ1720 which has a redshift (0.164) similar to those of lensing clusters (Mazzotta et al. 2001). Such motion may explain the offsets between X-ray and lensing centers. In a word, it seems that the consistency or discrepancy between the two mass estimates can be simply related to the question of whether or not the X-ray centers show a displacement from the central cD galaxies in lensing clusters.

In this paper, we present a Chandra observation of the lensing cluster Abell 1689 at redshift $z = 0.181$, in an attempt to reexamine the consistency/discrepancy between X-ray

and lensing mass estimates and the possible offset between X-ray and optical centers. The mass distribution of Abell 1689 has been reconstructed by several independent techniques of gravitational lensing: arcs and arclets (Tyson & Fischer 1995), the number count dilution of lensed red galaxies (Taylor et al. 1998), the distortion of background galaxy luminosity function (Dye et al. 2001) and the weak lensing of background galaxies (Clowe & Schneider 2001). This cluster was observed with *EINSTEIN*, *ROSAT*, *GINGA*, and *ASCA*. The X-ray luminosity in the 0.1 - 2.4 band is $(2.74 \pm 3.32) \times 10^{45}$ erg s⁻¹ (Ebeling et al. 1996) and the X-ray temperature is $T = 9.02_{-0.30}^{+0.40}$ keV (Mushotzky & Scharf 1997). The X-ray determined mass within the giant arc position ($\sim 51''$), under the assumption of hydrostatic equilibrium, is found to be lower by a factor of ~ 2 than that derived from strong gravitational lensing (Miralda-Escudé & Babul 1995; Wu & Fang 1997; Allen 1998; Wu 2000). In particular, based on the *ROSAT HRI* observation, Allen (1998) attributed this discrepancy to the offset of $13''.3$ between the lensing and X-ray centers. The offset value is within $1 - 2\sigma$ position uncertainty considering that *ROSAT HRI* provides a ~ 5 arcsec (full width at half-maximum) imaging resolution. With the new Chandra observation of Abell 1689, which is one magnitude improved in spatial resolution with respect to *ROSAT HRI*, we are now able to reexamine the reported mass discrepancy and its origin. Throughout this paper, we assume $H_0 = 50$ km s⁻¹ Mpc⁻¹ and $\Omega_0 = 1$.

2. Chandra observation and analysis

2.1. Data preparation

Abell 1689 was observed twice for separate 10 ksec by the Chandra X-ray Observatory on April 15, 2000 and January 7, 2001, respectively. Both observations were performed by using mainly the on board Advanced CCD Imaging Spectrometer in 2×2 imaging array (ACIS-I) mode. In the present work, the dataset is retrieved from the Chandra archive for

the first 10 ksec observation. The second observation, unfortunately, suffered from some serious aspect problem and the dataset has not yet been made available for public.

In order to achieve a better modeling of instrument gain and quantum efficiency, we process the Level 1 CXC data products using Chandra Interactive Analysis of Observations package CIAO-2.2, with complement of the updated calibration database CALDB-2.9. Following the standard methods (Chandra Science Threads for CIAO-2.2¹), we remove the Pixel and PHA Randomization effects, and “streak” events from the original event file.

Periods of background flaring are removed using the CIAO task **lc_clean** for ACIS chips I0-3 one by one. This finally yields an effective exposure time of ~ 7182 s after all known corrections for Abell 1689 are taken into account.

While the telescope pointing placed bulk of the cluster emission on the ACIS chip I3, a certain cluster emission also extends over other three adjacent chips. This may cause some problems in finding source-free background regions for the spatial and spectral analysis. Thus, a suitable blank-sky background dataset, `acisi_C_i0123_bg_evt_230301.fits`, compiled by Markevitch (2001) has been chosen and tailored for the present observation. We apply the same cleaning algorithm to the data as was applied to the background set. Identical spatial and energy filters are applied to source and background data so that the background normalization is set by the ratio of their exposure times. Moreover, we have created a spectral weighted exposure map (see section 2.2) for the entire ACIS chip array, using the aspect histogram files which contain information about aspect motion during the observation for each chip, and instrument maps which are essentially the product of detector quantum efficiency and mirror effective area projected onto the detector surface.

Figure 1 displays a true color image of Abell 1689, produced by a mosaic of three X-ray

¹available at http://asc.harvard.edu/ciao/documents_threads.html.

bands, red: 0.3–1.5 keV, green: 1.5–3 keV and blue: 3–10 keV. Images in each of the three bands, after being normalized by the exposure map, have been binned by four (such that an image pixel subtends 1.96 arcsec^2 on the sky) and adaptively smoothed using CIAO task *csmooth* at 3σ significant levels with a maximum smoothing scale of 5 pixels. It appears that with Chandra’s high spatial resolution a large number of X-ray point sources have been resolved within the field around the galaxy cluster, $\sim 16' \times 16'$.

In order to check the Chandra astrometry, we use the CIAO tool **wavdetect**, with a significance parameter value of 10^{-7} , to search for sources in the broad band image (0.3-10 keV) of the cluster field. A total of 29 sources are detected (see Figure 1). The source list is then compared with the optical USNO-A2.0 catalog and the radio FIRST catalog . Using a correlation radius of $1.5''$, we find three matches within a $12'$ radius of the ACIS-I center. The cumulative probability of a single random association between this data is 0.016. The probability that all the three matches occurred by chance is only 3.8×10^{-6} . Therefore, we conclude that the astrometry of this Chandra observation is not worse than $1''.5$ without further adjustments.

2.2. Spectral analysis

First we wish to work out the mean temperature and metallicity of the cluster. For this purpose, an overall spectrum within a large circular region of radius $3.7'$ (corresponding to a physical radius of 0.87 Mpc) has been extracted from the cleaned events after excluding several point sources. The resulted spectrum is further grouped so that each energy bin contains at least 20 counts. Because for energies below 0.7 keV uncertainties in the current available ACIS-I response functions are relatively large, our spectrum analysis is restricted to the 0.7-9 keV energy band. We fit the spectrum using the thermal emission model MEKAL with a fixed absorption at the Galactic value, $1.8 \times 10^{20} \text{ cm}^{-2}$. We find that this

model (hereafter Model 1) does not give the best description of the data reflected by $\chi^2/\text{d.o.f.} = 344/311$. The best fit of the data needs an additional absorption to the MEKAL model (hereafter Model 2), which improves the fit of Model 1 significantly at $> 99.9\%$ confidence level with $\chi^2/\text{d.o.f.} = 289/310$. The observed and fitted spectra of Abell 1689 are plotted in Figure 2, and the best fit parameters of both models are listed in Table 1. It turns out that although the resulting X-ray temperature depends sensitively upon whether or not there is an extra absorption component, the best fit value of metallicity remains almost unaffected. This last point can be seen in the confidence plot (Figure 3) of metallicity versus temperature. In summary, the average temperature and metal abundance for Abell 1689 are $kT = 8.2 - 10.0$ keV (or $11.0 - 14.7$ keV) and $Z = 0.20 - 0.49$ of solar, respectively. The bulk emission flux in the 0.5–10 keV band is $2.7 \pm 1.0 \times 10^{-11}$ ergs cm^{-2} s^{-1} , corresponding to an X-ray luminosity of $L_x = (4.12 \pm 1.53) \times 10^{45}$ erg s^{-1} in the 0.5–10 keV band or a bolometric X-ray luminosity of $L_x = (6.65 \pm 2.55) \times 10^{45}$ erg s^{-1} . This is in good agreement with the expected value from the statistical L_x - T relation for clusters (Wu, Xue & Fang 1999) when the flux falling out the detection aperture is included using the β model given below.

2.3. Temperature structure

Now we investigate the temperature structure of the cluster. We extract spectra for a series of annuli centered at the centroid of cluster emission (see section 2.4 for spatial analysis). All these spectra are properly grouped, which allows us to perform the minimum χ^2 analysis. Here, both Model 1 and Model 2 are used. Alternatively, in order to set a robust constraint on temperature value, we freeze the metallicity parameter in the fitting process. The results are summarized in Table 2 and the azimuthally averaged temperature profile is shown in Figure 4.

2.4. Surface brightness

In order to take the possible asymmetric emission distribution into account, we first model the bulk X-ray emission of the cluster with a two-dimensional β model in the form

$$S_x(x, y) = S(r) = \frac{S_{x0}(x_0, y_0)}{(1 + (r/r_c)^2)^\alpha}, \quad (1)$$

where

$$r(x, y) = \frac{\sqrt{x'^2(1 - \epsilon)^2 + y'^2}}{1 - \epsilon}, \quad (2)$$

and

$$x' = (x - x_0) \cos \theta + (y - y_0) \sin \theta, \quad (3)$$

$$y' = (y - y_0) \cos \theta + (x - x_0) \sin \theta. \quad (4)$$

The model assumes that cluster emission has a projected elliptical brightness surface with ellipticity ϵ and position angle θ . The surface brightness is measured in photon counts/arcsec²/s with respect to the X-ray centroid (x_0, y_0) , and is characterized by the core radius r_c and a power-law index α . We apply this model to the exposure corrected image of the cluster in 0.3-10 keV, and also include the blank field background. The best fit results are summarized in Table 3. It appears that the core radius is in the range of $r_c = 16''.6 - 18''.6$, the index α is 1.0–1.2, the normalization is $S_{x0} = (6.7 - 7.6) \times 10^{-6}$ photons cm⁻² s⁻¹, and the X-ray emission centroid is located at $\alpha = 13^h 11^m 29^s.45(\pm 3.45'')$, $\delta = -01^\circ 20' 28''.06(\pm 1.35'')$. Overall, the emission pattern is rather symmetric about the centroid with a very small value of ellipticity, $\epsilon = 0.08$.

We have performed a detailed check of the HST observations of Abell 1689, which clearly shows a central dominant cD galaxy, with the position coinciding nicely with the X-ray centroid within $\sim 1.5''$ uncertainties. We have then checked the FIRST observation in the radio band, which demonstrates a central emission peaked at

($13^h11^m30^s.002, -01^\circ20'28''.28$). This is about $8''$ from the X-ray emission centroid. A visual examination shows that the radio centroid is centered on one of the companion galaxies around the central cD. In Figure 5, we plot the X-ray emission contours overlaid on an HST/WFPC2 image of Abell 1689.

Since the X-ray emission of the cluster is fairly symmetric, we first employ the conventional single β model to fit the radial brightness profile of the cluster. However, the fitting is not acceptable, reflected by $\chi^2/\text{d.o.f} = 225.4/49$. We then adopt a double β model

$$S_x(r) = S_{x0}^1 \left(1 + \frac{r^2}{r_{c1}^2}\right)^{-3\beta_1+0.5} + S_{x0}^2 \left(1 + \frac{r^2}{r_{c2}^2}\right)^{-3\beta_2+0.5}, \quad (5)$$

which provides a significantly reduced χ^2 fit to the data with $\chi^2/\text{d.o.f} = 50.6/46$. The best fit parameters are summarized in Table 4, and the observed and fitted surface brightness profiles are demonstrated in Figure 6.

3. Mass determinations

Morphology of the overall X-ray surface brightness distribution of A1689, along with the nearly constant temperature across the cluster surface out to $r \sim 1$ Mpc, suggests that Abell 1689 is a dynamically-relaxed cluster. This argument is further supported by the fact that the X-ray centroid coincides with the central dominant cD galaxy. Consequently, one may use the hydrostatic equilibrium hypothesis to evaluate the dynamical mass of the cluster. For an isothermal, double β model, the total dynamical mass within radius R can be obtained from

$$M(R) = -\frac{kTR^2}{G\mu m_p n(R)} \left[\frac{dn_1(R)}{dR} + \frac{dn_2(R)}{dR} \right], \quad (6)$$

where $\mu = 0.59$ is the average molecular weight, $n_i(R)$ ($i=1,2$) is the particle number density for the i th phase gas and $n(R) = n_1(R) + n_2(R)$. By reverting the observed surface brightness distribution $S_x(r)$ [equation (5)], we can derive an analytic expression for $n_i(R)$

(Xue & Wu 2000). Next, we infer the mass density profile from $\rho(R) = (1/4\pi R^2)[M(R)/dR]$, and calculate the projected mass $m(r)$ within radius r from the cluster center along the line-of-sight. The resulting mass distribution based on the average temperature of $T = 13.2^{+1.5}_{-1.2}$ from Model 1 is shown in Figure 7. Note that utilization of Model 1 yields a maximum estimate of the X-ray cluster mass because the temperature given by Model 1 is significantly higher than that by Model 2.

On the other hand, the projected cluster mass within the position of giant arc r_{arc} can be estimated through

$$m(r_{\text{arc}}) = \pi r_{\text{arc}}^2 \Sigma_{\text{crit}}, \quad (7)$$

where $\Sigma_{\text{crit}} = (c^2/4\pi G)(D_s/D_d D_{\text{ds}})$ is the critical surface mass density, D_d , D_s and D_{ds} are the angular diameter distances to the cluster, to the background galaxy, and from the cluster to the galaxy, respectively. Unfortunately, the redshift of the giant arc at $51''$ from the cD galaxy of Abell 1689 remains unknown. Assuming $z_s = 0.8$ and $z_s = 2.0$ for the arc in the above equation yields $m(r_{\text{arc}}) = 3.76 \times 10^{14} M_{\odot}$ and $m(r_{\text{arc}}) = 3.18 \times 10^{14} M_{\odot}$, respectively. For comparison, the X-ray cluster mass within r_{arc} derived from the Chandra data reads $m(r_{\text{arc}}) = 2.44^{+0.25}_{-0.20} \times 10^{14} M_{\odot}$ and $m(r_{\text{arc}}) = 1.66^{+0.21}_{-0.10} \times 10^{14} M_{\odot}$ for Model 1 and Model 2, respectively. Namely, the ratios of strong lensing masses to X-ray masses given by spectral Model (1, 2) within r_{arc} are $(1.54^{+0.14}_{-0.14}, 2.27^{+0.15}_{-0.26})$ and $(1.30^{+0.12}_{-0.12}, 1.92^{+0.11}_{-0.22})$ for $z_s = 0.8$ and $z_s = 2.0$, respectively. All the quoted errors are 90% confidence limits. Recall that previous estimates based on the *ROSAT* and *ASCA* data ($T \approx 9.0$ keV) found a mass ratio of ~ 2 (Allen 1998; Wu 2000), which is in good agreement with our results based on Model 2. In other words, the high resolution observation of Chandra yields essentially the same result of X-ray cluster mass in the central core of Abell 1698. Only for Model 1 can the mass discrepancy be reduced especially when the background source is assumed at large redshifts and the measurement uncertainties are included.

The projected mass distribution of Abell 1689 has also been obtained from the study of the deficit of red galaxies behind the cluster by Taylor et al. (1998). We illustrate their reconstructed mass profile in Figure 7, allowing the uncertainties to include 90% confidence limits. Another mass estimate is provided by Dye et al. (2001) from the comparison of luminosity functions of background galaxies between the lensed field behind Abell 1689 and an undistorted control field. Their cumulative projected masses within three radii are shown in Figure 7. Finally, Clowe & Schneider (2001) fitted their weak lensing derived cluster masses to a singular isothermal sphere for a set of assumed background galaxy redshifts, which are also demonstrated in Figure 7. It appears that the overall projected cluster masses reconstructed by four different lensing methods (arcs, number counts, distorted luminosity function of galaxies and weak lensing analysis) show a good agreement within measurement uncertainties.

The newly determined mass of Abell 1689 in the central region of $r \approx 0.2$ Mpc by Chandra observation is systematically lower than those derived from strong and weak lensing techniques, although the two innermost data points given by the distorted luminosity function of galaxies are still consistent with the projected X-ray mass when the large measurement uncertainties are included. Nevertheless, at large radii $r > 0.6$ Mpc the two mass estimates yield roughly the same result.

4. Discussion and conclusions

The high spatial resolution observation of Abell 1689 with Chandra has permitted an accurate localization of the X-ray centroid of the cluster, which shows a perfect coincidence with the central cD galaxy, suggesting that the cluster has become fully relaxed at its redshift $z = 0.181$. The central cooling time within $r = 10$ kpc is $t_{\text{cool}} = 2.54^{+0.20}_{-0.17}$ Gyr and the cooling radius is $r_{\text{cool}} = 150$ kpc. The newly determined X-ray surface brightness

and temperature distributions, incorporated with the hydrostatic equilibrium hypothesis, have allowed us to re-evaluate the projected mass profile of the cluster and compare it with the results provided by different lensing techniques. It shows that the significant mass discrepancy between X-ray and lensing methods reported in previous studies still remains even if the new Chandra data are used.

With the unprecedented sub-arcsec spatial resolution, as well as the large effective detection areas in the broad energy range of 0.3-10 keV, the new Chandra observation of Abell 1689 disagrees with previous findings based on *ROSAT* observation that there exists an offset of $13''.3$ between the X-ray and optical centers (Allen 1998). The latter was suggested to be the main cause for the discrepancy between X-ray and lensing mass estimates. Indeed, the presence of such offset is a good indicator of local violent activities of the intracluster gas in the central core so that hydrostatic equilibrium may become inapplicable. An alternative is that the offset is produced by the oscillation of the central cD galaxy around the bottom of the cluster potential well (Lazzati & Chincarini 1998). The perfect coincidence between the X-ray center and the cD galaxy of Abell 1689 detected by Chandra observation, if it is not a projection effect, and the central mass discrepancy between X-ray and lensing measurements pose a challenge to the above speculation. If confirmed, this would have significant impacts on our understanding of the distribution and evolution of intracluster gas in the central cores of clusters. Future observations of other lensing clusters with Chandra would clarify the issue.

We thank the referee for constructive suggestions. This work was supported by the National Science Foundation of China, under Grant No. 19725311 and the Ministry of Science and Technology of China, under Grant No. NKBRSF G19990754.

REFERENCES

- Allen, S. W. 1998, MNRAS, 296, 392
- Allen, S. W., Ettori, S., & Fabian, A. C. 2001, MNRAS, 324, 877
- Arabadjis, J. S., Bautz, M. W., & Garmire, G. P. 2001, ApJ, submitted
- Clowe, D., & Schneider, P. 2001, A&A, in press
- Dye, S., et al. 2001, MNRAS, 321, 685
- Ebeling, H., et al. 1996, MNRAS, 281, 799
- Katayama, H., Hayashida, K., & Hashimoto, K. 2002, PASJ, in press
- Lazzati, D., & Chincarini, G. 1998, A&A, 339, 52
- Machacek, M. E., Bautz, M. W., Canizares, C., & Carmire, G. P. 2001, ApJ, submitted
- Markevitch, M. 2001,
http://asc.harvard.edu/cal/Links/Acis/acis/Cal_prods/bkgrnd/current/index.html
- Mazzotta, P., et al. 2001, ApJ, 555, 205
- Miralda-Escudé, J., & Babul, A. 1995, ApJ, 449, 18
- Mushotzky, R. F., & Scharf, C. A. 1997, ApJ, 482, L13
- Schmidt, R. W., Allen, S. W., & Fabian, A. C. 2001, MNRAS, 327, 1057
- Taylor, A. N., Dye, S., Broadhurst, T. J., Benítez, N., & van Kampen, E. 1998, ApJ, 501,
539
- Tyson, J. A., & Fitchner, P. 1995, ApJ, 446, L55
- Wu, X.-P. 1994, ApJ, 436, L115
- Wu, X.-P. 2000, MNRAS, 316, 299
- Wu, X.-P., Chiueh, T., Fang, L.-Z., & Xue, Y.-J. 1998, MNRAS, 301, 861

Wu, X.-P., & Fang, L.-Z. 1997, ApJ, 483, 62

Wu, X.-P., Xue, Y.-J., & Fang, L.-Z. 1999, ApJ, 524, 22

Xue, Y.-J., & Wu, X.-P. 2000, MNRAS, 318, 715

Table 1. Average Emission properties of Abell 1689

Model	N_{H} (10^{20}cm^{-2})	Temperature (keV)	Metallicity (Z_{\odot})	$\chi^2/\text{d.o.f}$
Model 1	-	$13.2^{+1.5}_{-1.2}$	$0.35^{+0.14}_{-0.15}$	344/311
Model 2 ^a	$6.7^{+1.5}_{-1.5}$	$9.0^{+1.0}_{-0.8}$	$0.31^{+0.10}_{-0.09}$	289/310

^aObserved flux in 0.5-10 keV, $2.7^{+0.1}_{-0.1} \times 10^{-11}$ ergs cm^{-2} s^{-1} .

Note. — All the fittings have a fixed absorption at the Galactic value. All the errors quoted are at the 90% confidence level (i.e. $\Delta\chi^2 = 2.7$).

Table 2. Temperature structures of Abell 1689

Annuli(")	Net counts	T_1^a (keV)	T_2^a (keV)
0-10	1197	14.5(10.4-20.8)	9.7(7.1-13.8)
10-20	2074	8.7(7.3-10.5)	7.8(6.7-9.3)
20-30	1818	9.1(7.6-11.5)	7.6(6.5-9.2)
30-40	1219	17.6(12.5-24.3)	14.3(9.2-17.1)
40-50	1388	12.4(9.2-16.4)	8.8(6.9-11.1)
50-70	1804	11.8(9.2-15.7)	8.5(7.0-10.8)
70-80	921	14.3(10.0-21.8)	11.3(8.0-16.7)
80-115	1850	13.5(10.4-18.2)	9.8(8.0-12.6)
115-155	1521	14.8(11.1-20.6)	12.9(9.6-17.6)

^aTemperature values are from Model 1 and Model 2, respectively. The intervals in parentheses represent 90% confidence limits.

Table 3. 2-dimensional Modeling of the surface brightness profile of Abell 1689

r_c (")	α	S_{x0} (photons $\text{cm}^{-2} \text{s}^{-1}$)	x_0, y_0 (α, δ)	ϵ	θ (degree)
17.6 ± 1.0	1.1 ± 0.1	$(7.1 \pm 0.5) \times 10^{-6}$	$13^h 11^m 29^s .45(\pm 3.45''), -01^\circ 20' 28'' .06(\pm 1.35'')$	0.08	1.7

Table 4. Double β Modeling of the surface brightness profile of Abell 1689

r_{c1} (")	β_1	S_{x0}^1 (photons $\text{cm}^{-2} \text{s}^{-1}$)	r_{c2} (")	β_2	S_{x0}^2 (photons $\text{cm}^{-2} \text{s}^{-1}$)
20.6 ± 0.4	0.72 ± 0.01	$(4.1 \pm 0.1) \times 10^{-7}$	90.0 ± 1.0	0.87 ± 0.01	$(4.5 \pm 0.1) \times 10^{-8}$

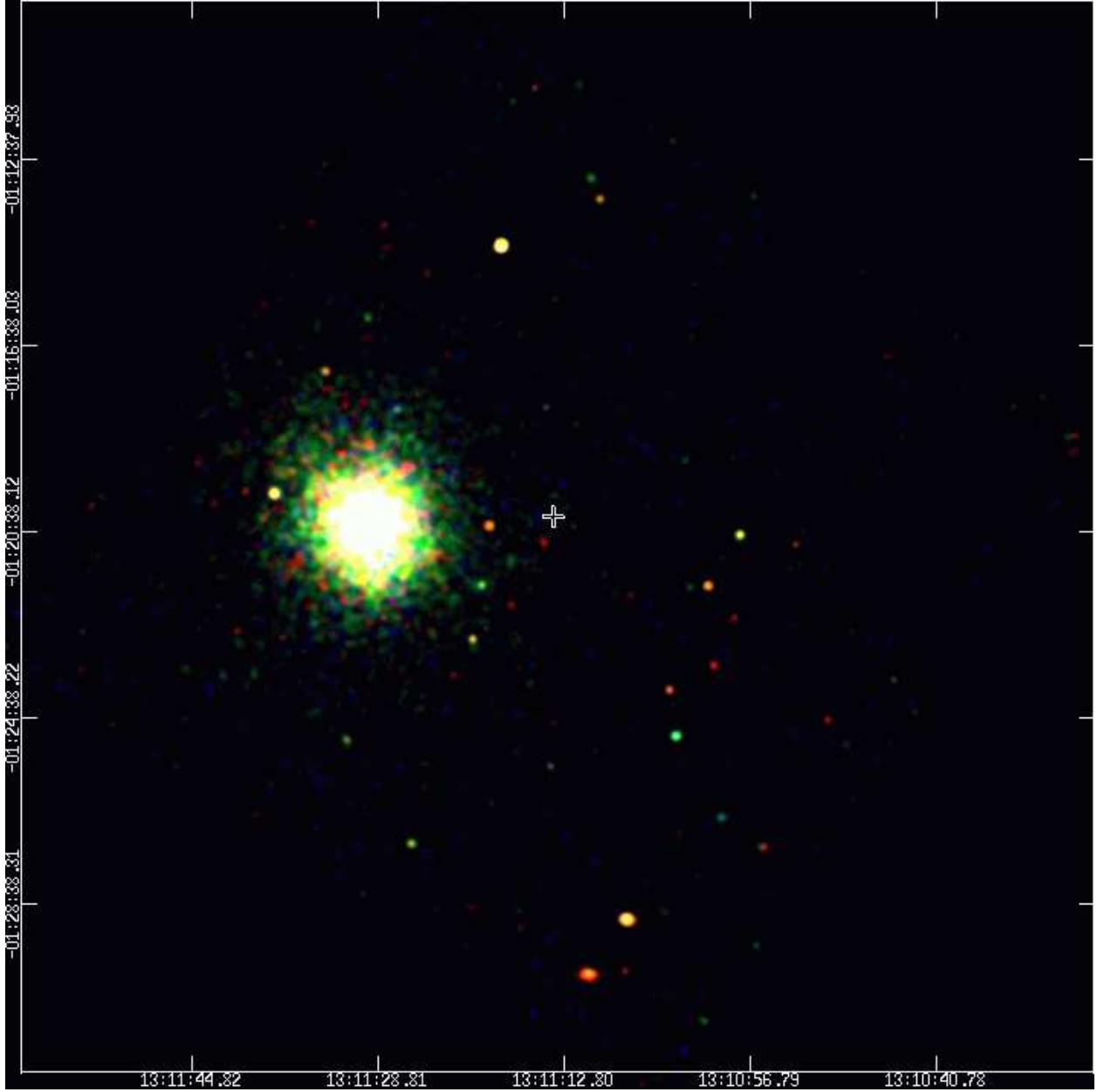


Fig. 1.— True color image of Abell 1689, produced by a mosaic of three smoothed X-ray bands: red: 0.3–1.5 keV; green: 1.5–3 keV; and blue: 3–10 keV. Numerous X-ray point sources have been resolved within the field around the galaxy cluster, $\sim 16' \times 16'$.

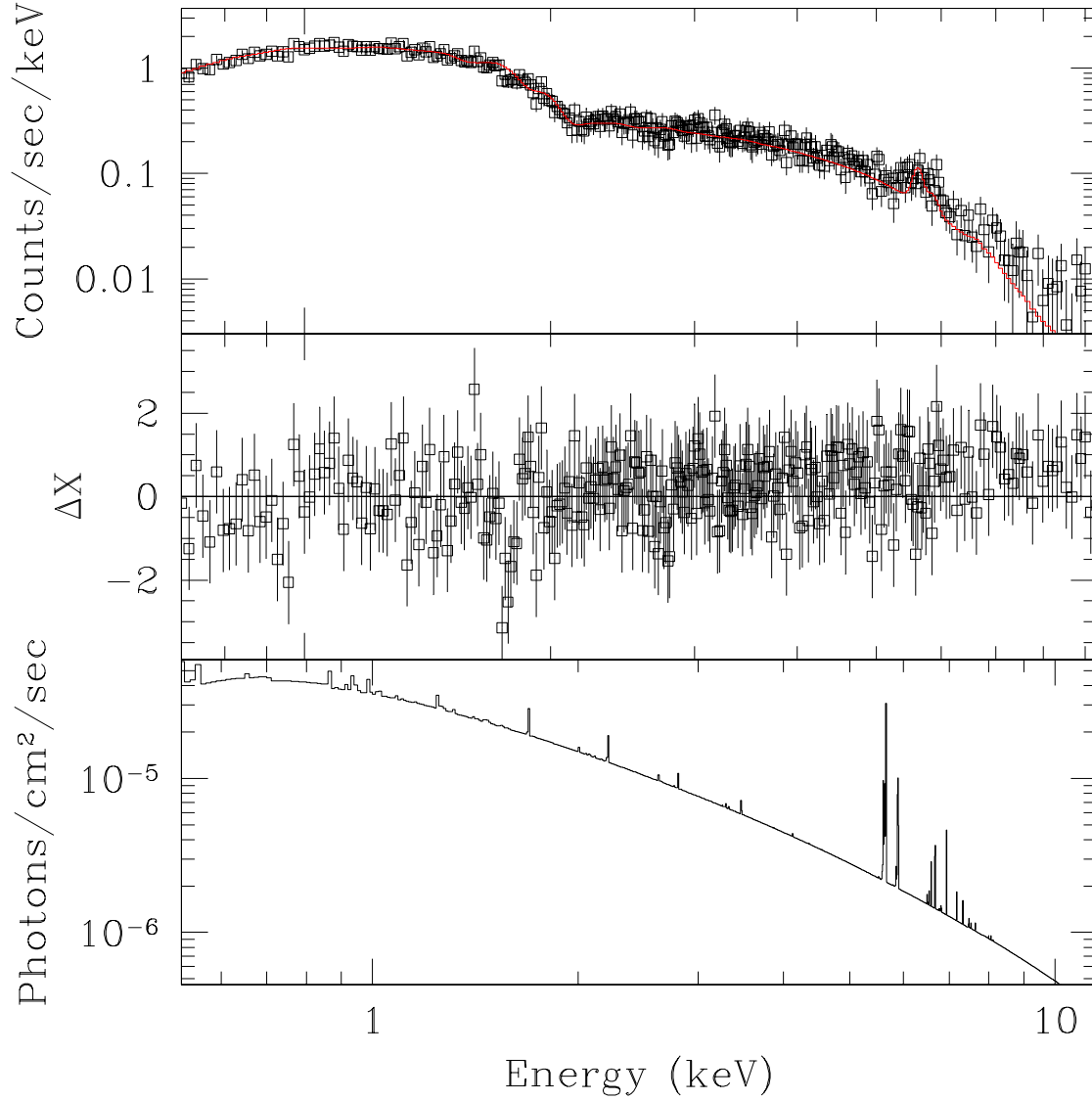


Fig. 2.— Observed X-ray spectrum of Abell 1689 (upper panel) fitted by the thermal emission model MEKAL with an excess absorption (Model 2, bottom panel) convolved with Chandra instrumental responses. The fitting residuals are shown in the middle panel.

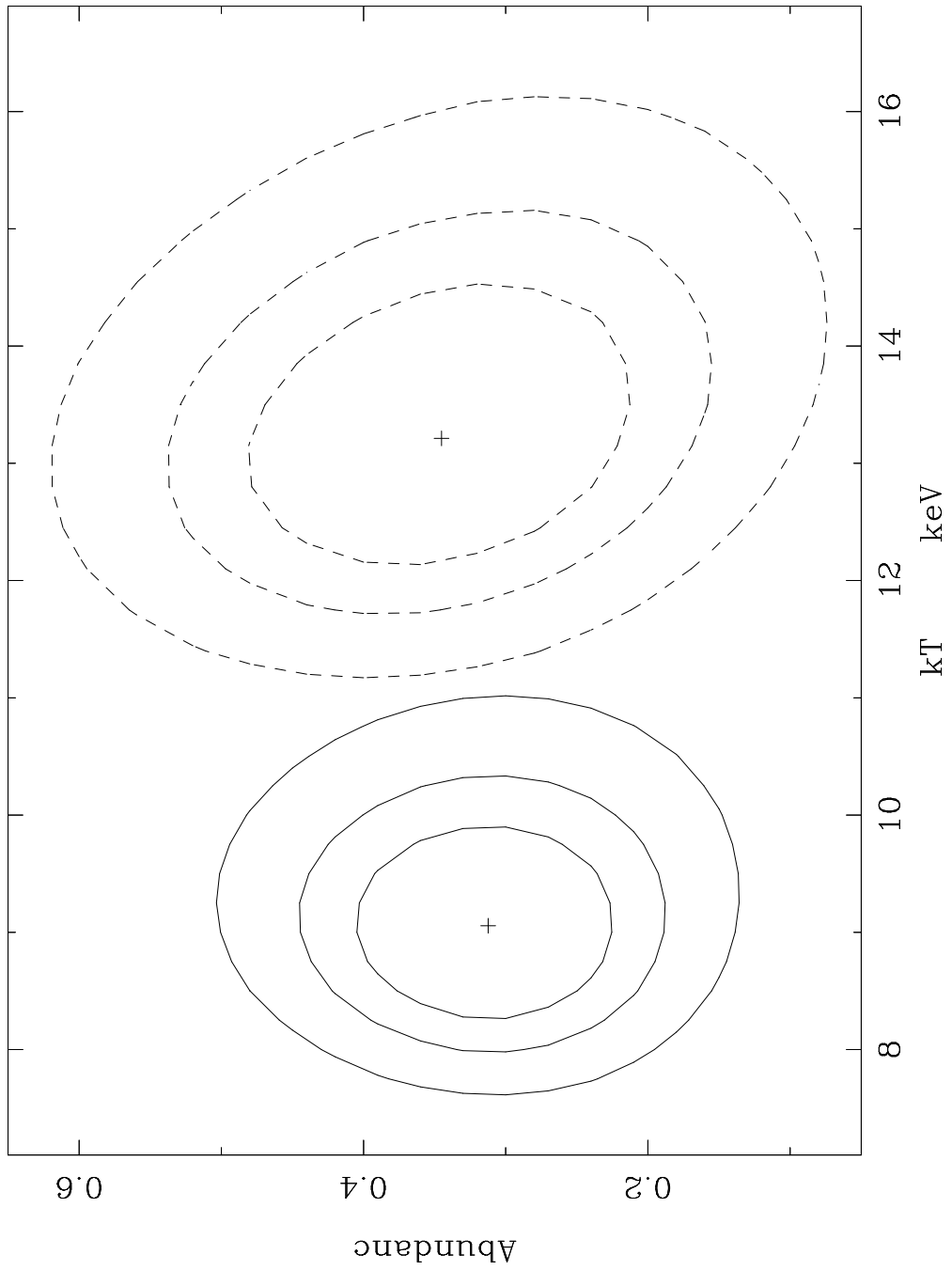


Fig. 3.— Confidence plot (68%, 90%, and 99%) of metallicity versus temperature for bulk thermal emissions of Abell 1689. Dashed-line and solid-line contours are for Model 1 and Model 2, respectively.

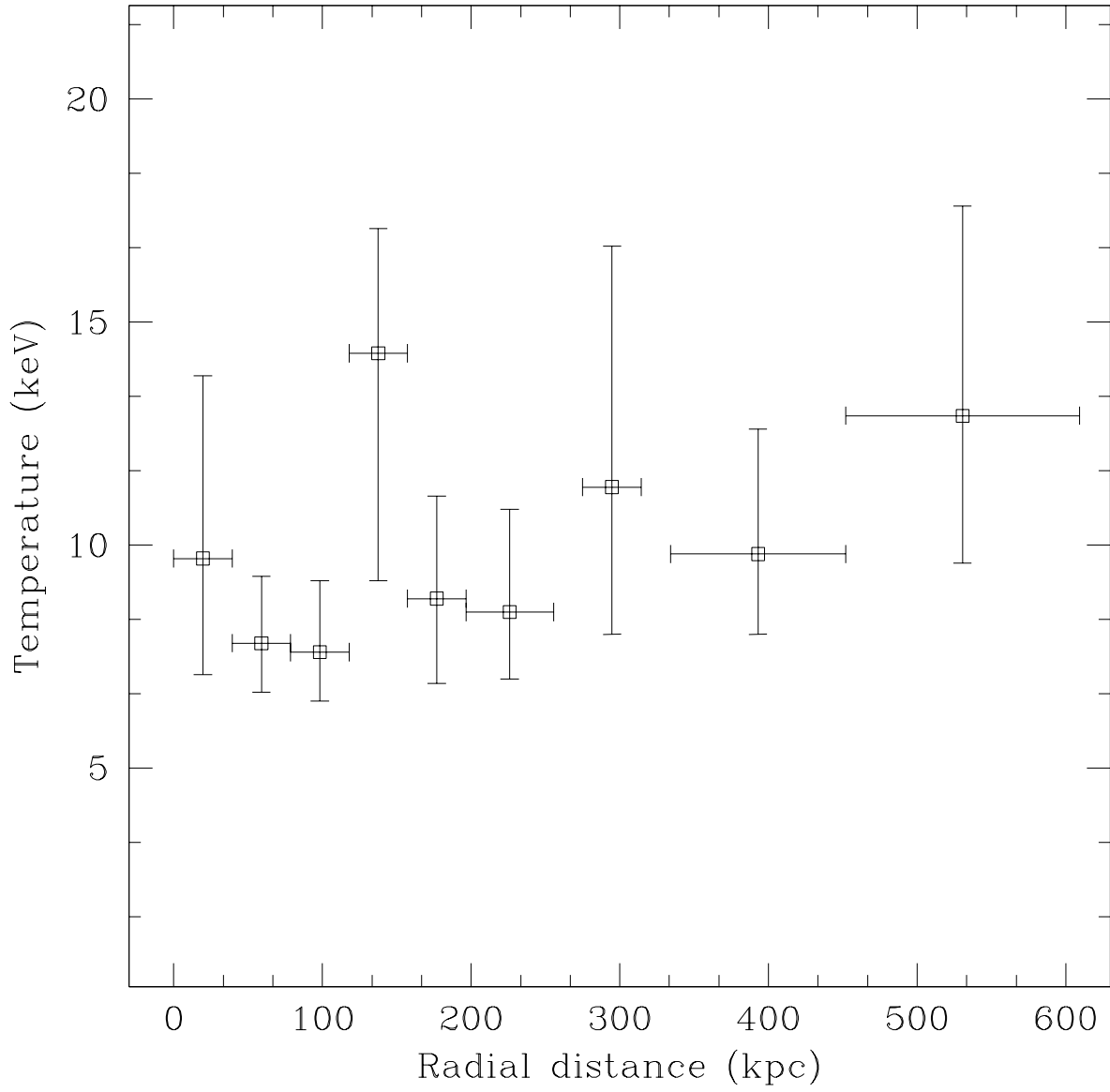


Fig. 4.— Temperature profile of Abell 1689 constructed from Model 2.

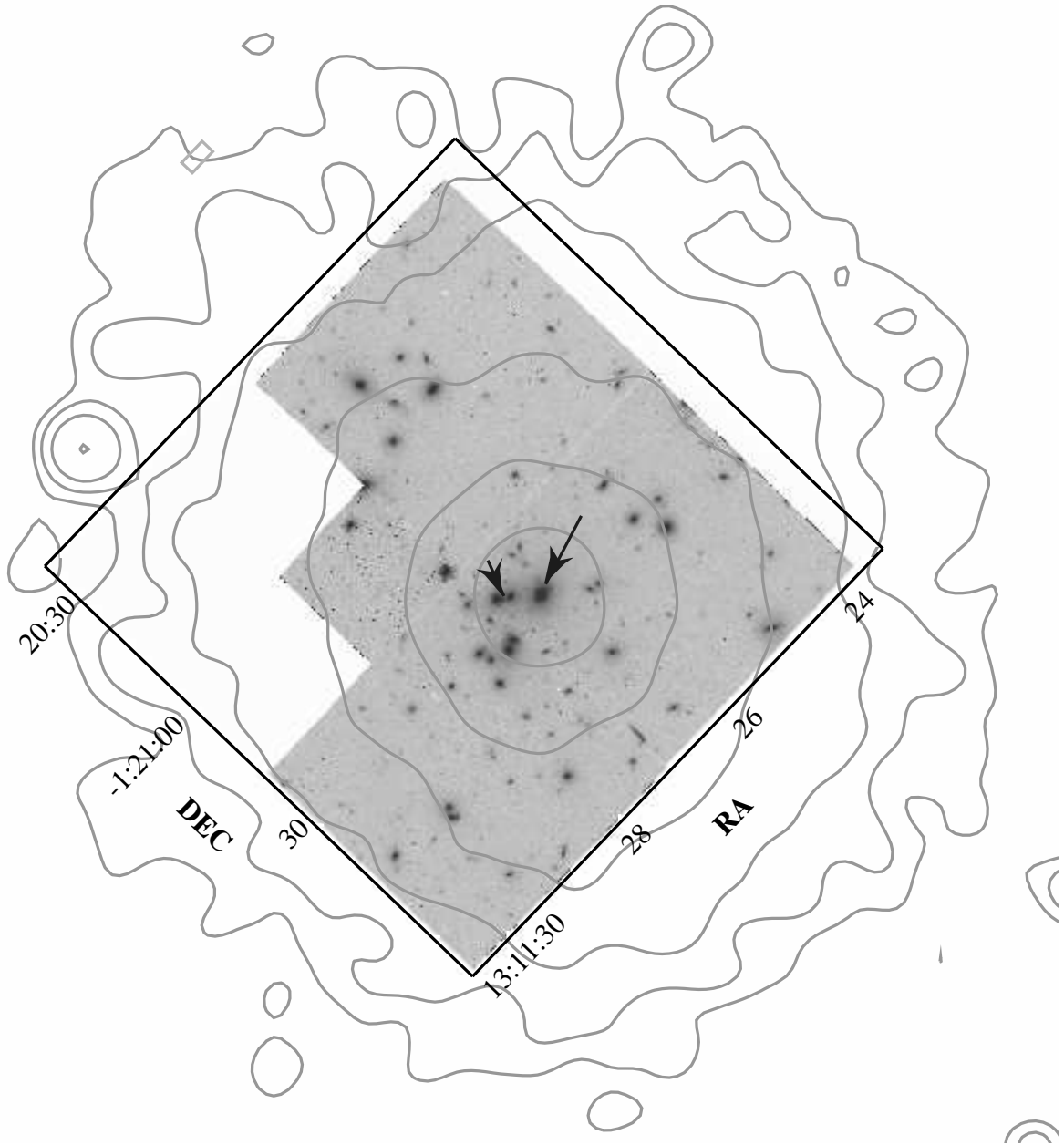


Fig. 5.— X-ray emission contours overlaid on an HST/WFPC2 image of the central region of Abell 1689. Up is the North and left is to the East. Note that the central cD galaxy of the cluster, as indicated by the big arrow, coincides perfectly with the X-ray emission centroid. The small arrow points the position of the radio (FIRST) peak.

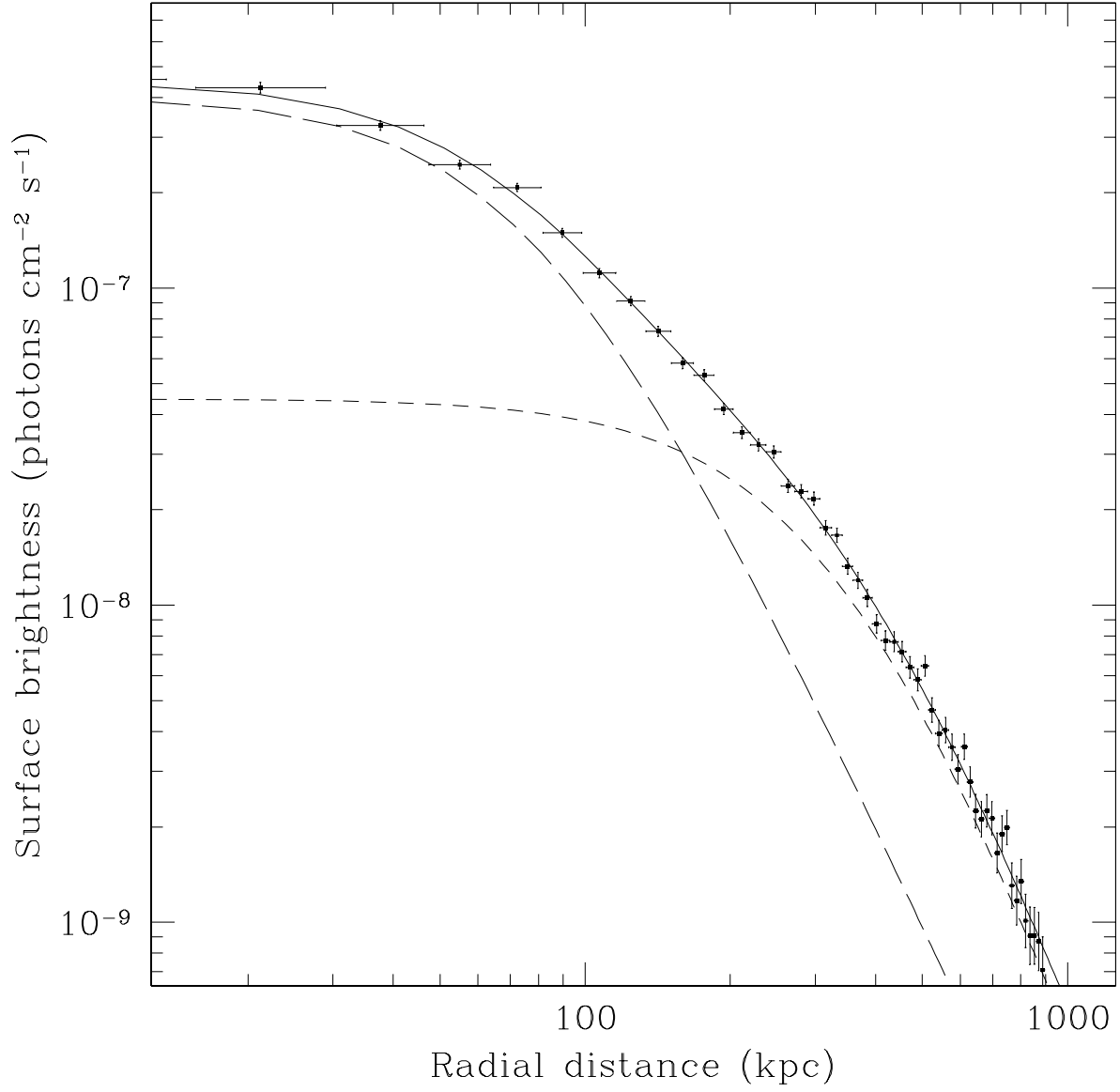


Fig. 6.— Observed radial profile of X-ray surface brightness, together with the double β model fitting.

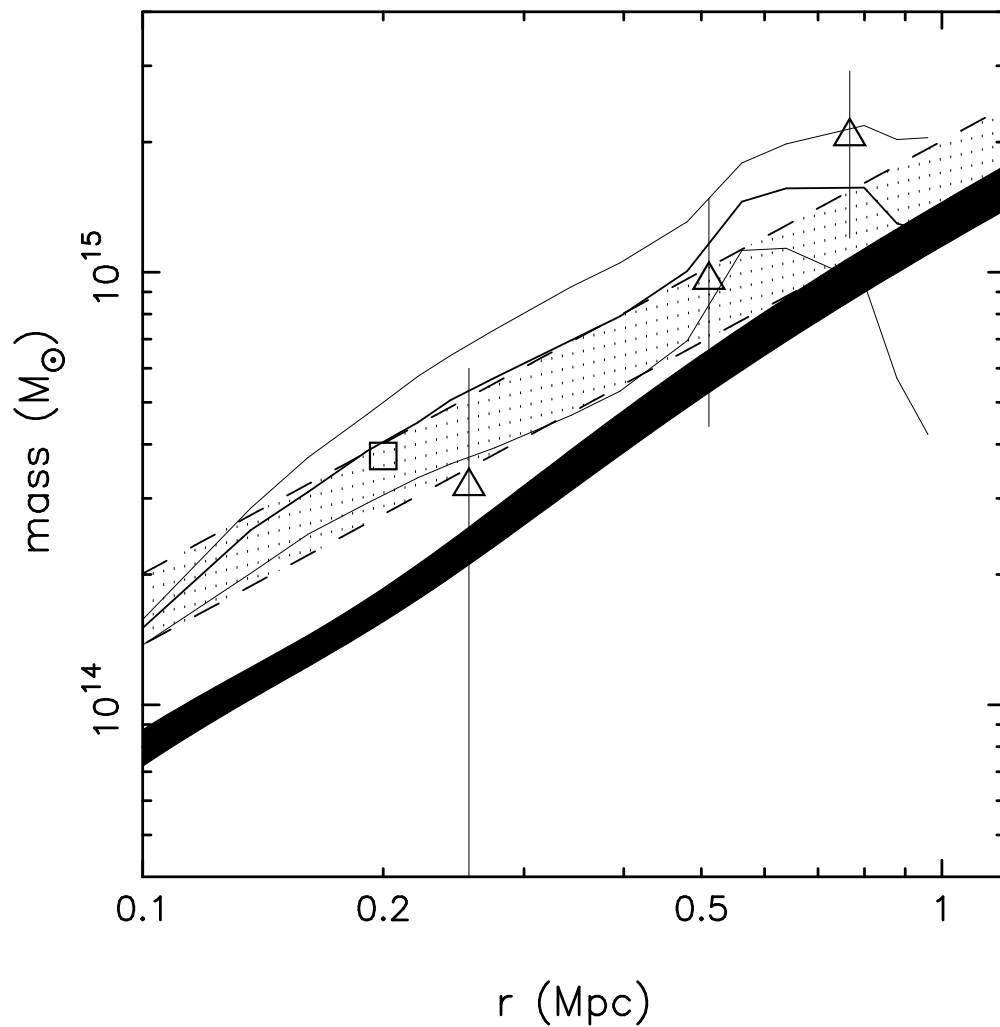


Fig. 7.— Projected mass distributions of Abell 1689 derived from the Chandra observation (filled region with 90% confidence limits), the strong gravitational lensing (square), the distortion of background galaxy luminosity function (triangles), the deficit of number counts of red galaxies (solid lines) and the best fit singular isothermal sphere to the weak lensing data for background galaxy redshifts from $z = 0.5$ to 3.0 (dashed lines).